GFZ
Helmholtz-Zentrum
POTSDAM

HELMHOLTZ-ZENTRUM POTSDAM
DEUTSCHES
GEOFORSCHUNGSZENTRUM

Avellaneda-Jiménez, D. S., Monsalve, G., León, S., Gomez Garcia, A. M. (2022): Insights into Moho depth beneath the northwestern Andean region from gravity data inversion. - Geophysical Journal International, 229, 3, 1964-1977.

https://doi.org/10.1093/gji/ggac041

Institional Repository GFZpublic: https://gfzpublic.gfz-potsdam.de/

Geophysical Journal International

Geophys. J. Int. (2022) **229,** 1964–1977
Advance Access publication 2022 February 03
GJI Gravity, geodesy and tides

https://doi.org/10.1093/gji/ggac041

Insights into Moho depth beneath the northwestern Andean region from gravity data inversion

D.S. Avellaneda-Jiménez,[1] G. Monsalve,[2] S. León[1,3] and A.M. Gómez-García[4]

[1]*Departamento de Materiales y Minerales, Universidad Nacional de Colombia, Medellín, 050034, Colombia. E-mail: dsavellanedaj@unal.edu.co*
[2]*Departamento de Geociencias y Medio Ambiente, Universidad Nacional de Colombia, Medellín, 050034, Colombia*
[3]*Smithsonian Tropical Research Institute, Balboa, Ancon, 07098, Republic of Panama*
[4]*GFZ German Research Centre for Geosciences,* 14473 *Potsdam, Germany*

Accepted 2022 February 1. Received 2022 January 28; in original form 2021 August 9

SUMMARY

The complex Moho topography beneath the northwestern Andes is the result of multiple geodynamic processes during the Cenozoic. To contribute to our understanding of the Moho depth distribution beneath this region, we inverted gravity data from two widely used satellite-derived data sets (EGM2008 and EIGEN-6C4) and one regional airborne Bouguer gravity anomaly map (ANH2010). Their inversion allowed choosing the ANH2010, based on lower residual gravity and a higher agreement with seismic estimations, as the most suitable data set to gain insights into the Moho depth beneath the northwestern Andes and its relationship with previously identified tectonic features. The inverted Moho argues for a 40–50 km depth beneath the Central and Eastern cordilleras, reaching depths beyond 50 km below the Eastern Cordillera, and shallower depths between 30 and 40 km mainly along the foreland region to the east, the Western Cordillera and the coastal plains. Three main thickened crust features of regional extent were identified: (1) a deep Moho expression with a crustal thickness greater than 40 km in the northwesternmost foreland region, which we consider a direct consequence of the adjacent thickened Eastern Cordillera involving the fold and thrust deformation migration from the range towards the foreland, and the flexural deformation proposed for the eastern foothills; (2) a regional deep Moho expression (50–60 km) along the axis of the Eastern Cordillera, related to its shortening history including multiple phases of Cenozoic thick-skinned deformation and magmatic underplating; and (3) a Moho deeper than 60 km in a southern latitude (1°S–1°N) beneath the modern magmatic arc, whose interpretation is more complex, likely a combined result of mafic addition to the base of the crust, foundering tectonics, and lateral displacement of the lower crust prompted by the subducting Carnegie ridge.

Key words: Structure of the Earth; Satellite gravity; South America; Inverse theory; Dynamics: gravity and tectonics.

1 INTRODUCTION

The Moho discontinuity is defined as the rheological boundary where seismic velocity sharply increases due to the transition from crustal to mantle materials (Mooney 2021). This boundary can be complex in terms of depth and geometry along active orogens since it is subjected to physical and chemical processes promoted by the interaction between the base of the crust and the underlying uppermost mantle (Larkin *et al.* 1997; Schreiber *et al.* 2010; Karabulut *et al.* 2013; Kay *et al.* 2014). In subduction-related orogens, as the northwestern Andean region, the complexity of the crust–mantle transition depends on its petrologic contrast, lateral compositional and thermal dissimilarity, underplating and/or delaminating processes, and lower crustal flow, affecting the isostatic equilibrium as well as the rheological response of the overlying crust (Beck & Zandt 2002; Aitken *et al.* 2013; Spada *et al.* 2013; Shi *et al.* 2020; Xuan *et al.* 2020).

In the case of the northwestern Andes, a complex Moho topography is expected because of multiple tectonic processes that have occurred especially during the Cenozoic. They include the installation of different magmatic arcs during the Palaeogene currently juxtaposed by accretionary tectonics (Cardona *et al.* 2018; Montes *et al.* 2019), the development of an Oligo-Miocene to recent times magmatic arc installed above an accretionary orogen (Marín-Cerón

© The Author(s) 2022. Published by Oxford University Press on behalf of The Royal Astronomical Society.

Downloaded from https://academic.oup.com/gji/article/229/3/1964/6521443 by Geoforschungszentrum Potsdam user on 18 May 2022

et al. 2019; Monsalve-Bustamante 2020), the subduction zone migration of two different oceanic plates (Caribbean and Farallon) during the Cretaceous–Palaeogene, and the subsequent fission of the Farallon plate into Nazca and Cocos plate around 23 Ma ago (Lonsdale 2005), the collision of the Panama-Chocó arc during the early-middle Miocene (León *et al.* 2018; Montes *et al.* 2019), and the subsequent establishment of a subducting Caribbean plate to the north and Nazca plate to the west of the northwestern Andes, with changes in the subduction angle and slab tearing along-strike within those slabs (Chiarabba *et al.* 2015; Syracuse *et al.* 2016; Wagner *et al.* 2017; Vargas 2020). Moreover, receiver functions and petrologic constraints have suggested the presence, in multiple regions below the cordilleran belt, of crustal thicknesses above 55 km, high Vp/Vs ratios, and fast seismic velocities at the crust–mantle transition, which are interpreted as reflecting mafic underplating and foundering tectonics (Poveda *et al.* 2015; Bloch *et al.* 2017; Monsalve *et al.* 2019). Such mechanisms are expected to drive important modifications in the mantle structure and along the Moho interface (Beck & Zandt 2002; Thybo & Artemieva 2013).

In consequence, Moho topography beneath the northwestern Andes must be investigated from different approaches to improve our understanding of its spatial distribution and the relationship with modern and ancient tectonics. In this sense, the most reliable approach for estimating Moho depth is considered to be seismic imaging, which permits the determination of broad and fine structures along this discontinuity (Mooney 2021). Nevertheless, the resolution and accuracy of such an approach strongly depend on the coverage and distribution of seismic stations. To overcome this limitation, inversion of gravity data has been widely applied to complement the study of the Moho topography, showing good correlations with seismic-based estimations (Aitken *et al.* 2013; Prasanna *et al.* 2013; van der Meijde *et al.* 2013; Sahoo & Pal 2021). The advantage of using gravity lies in its wider coverage and data accessibility, which makes it a valuable approach to constrain the structure of the lower crust and uppermost mantle in regions with limited coverage of seismic monitoring, such as the study area. Yet, because different gravity data sets with contrasting spatial resolution and coverage are available, a comparison between obtained inversions must be done before any interpretation is proposed. Previous attempts in this regard have been made on a continental scale (van der Meijde *et al.* 2013; Uieda & Barbosa 2017) overlooking particularities of the northwestern Andes because of different scopes.

In this paper, we contribute to the understanding of the Moho depth beneath the northwestern Andes by initially inverting gravity data from two widely used satellite-derived data sets, that is EGM2008 (Pavlis *et al.* 2012) and EIGEN-6C4 (Förste *et al.* 2014; Ince *et al.* 2019), and one regional airborne Bouguer gravity anomaly map built by the National Hydrocarbon Agency of Colombia (Graterol & Vargas 2010). We followed the computation of a 3-D geometry of an interface with a crust–mantle density contrast, through the application of the Parker-Oldenburg iterative approach (Gómez-Ortiz & Agarwal 2005). We examine their differences in terms of convergence of the applied algorithm, their discrepancies with respect to global Moho models, that is CRUST1.0 (Laske *et al.* 2013) and GEMMA (Reguzzoni & Sampietro 2015), and their consistency with seismic constraints. By using an appropriate combination of parameters, after choosing the most suitable data set based on lower residual gravity and a higher agreement with seismic estimations, insights into Moho depth are discussed focusing on particular regional-extent expressions and their spatial correspondence with identified tectonic features.

2 TECTONIC SETTING

The Colombian Andes include three main mountain ranges named Eastern (EC), Central (CC) and Western Cordilleras (WC); the Magdalena Valley lies between EC and CC, and the Cauca-Patía Valley between CC and WC (Fig. 1). The foreland region lies to the east of the EC bounded by the dextral-reverse East Andean fault zone (Kellogg *et al.* 2019), composed of several individual thrusting fault systems (Veloza *et al.* 2012).

Slabs from at least two oceanic plates subduct beneath the Colombian Andes, the Caribbean plate to the north, beneath the Caribbean plains (CP in Fig. 1), and the Nazca plate to the west, beneath the Pacific plains and WC (Fig. 1). At 5–5.5°N, the so-called Caldas tear separates a flat-slab setting to the northwest, characterized by the absence of active volcanism, from normal/steep subduction to the south, where the modern magmatic arc is located (Vargas & Mann 2013; Chiarabba *et al.* 2015; Syracuse *et al.* 2016; Wagner *et al.* 2017; Vargas 2020).

Lithospheric thickness estimates of ∼103 km within the foreland region and ∼100–110 km along the Colombian Andes have been obtained from receiver functions, with no major latitudinal variations (Blanco *et al.* 2017). In terms of crustal thickness, seismic constraints suggest a 22–48-km-thick crust at the eastern foothills and the foreland region, and 20–40 km at the WC (Monsalve *et al.* 2013; Poveda *et al.* 2015). A crust thicker than 50 km is suggested beneath the central-northern region of the CC and EC (4–6°N), and along the southern CC (1–3°N; Poveda *et al.* 2015). Below the central EC, the identification of a high seismic velocity layer at the base of the crust has been interpreted as magmatic underplating, which seems to contribute to crustal thickening in this part of the orogen (Monsalve *et al.* 2019).

In terms of gravity data and modelling, along the CC, EC and the foreland region, Bouguer gravity anomalies correlate well with a continental-affinity crust (Case *et al.* 1971; Vargas & Mann 2013; Kellogg *et al.* 2019; Gómez-García *et al.* 2021). The WC is characterized by higher gravity anomalies (e.g. Case *et al.* 1971) due to the nature of the basement (oceanic crust) mostly associated with fragments of the Caribbean plate (Kerr *et al.* 1997) accreted during the latest Cretaceous to Palaeogene (Villagómez & Spikings 2013; Pardo-Trujillo *et al.* 2020; León *et al.* 2021). Beneath the Caribbean plains, integrated geological, seismic and gravity data suggest the presence of accreted mafic materials related to the Caribbean plate as well (Cardona *et al.* 2012; Vargas & Mann 2013; Bernal-Olaya *et al.* 2015).

3 METHODOLOGY AND ANALYSIS

3.1 Inversion code and gravity data sets

3.1.1 Gravity Moho inversion

To estimate Moho topography by means of gravity data inversion, we initially assume isostatic equilibrium and applied the 3DINVER.M code implemented by Gómez-Ortiz & Agarwal (2005). We consider isostatic equilibrium to be a good assumption since only positive residual topography has been considered for the northern Eastern Cordillera (Yarce *et al.* 2014; Siravo *et al.* 2018) with an amount of excess topography that we will show, is within the uncertainty of the applied method. The inversion code is based on the original equation of Parker (1973), who derived the Fourier transform of the gravitational field for an undulated interface in between

Downloaded from https://academic.oup.com/gji/article/229/3/1964/6521443 by Geoforschungszentrum Potsdam user on 18 May 2022

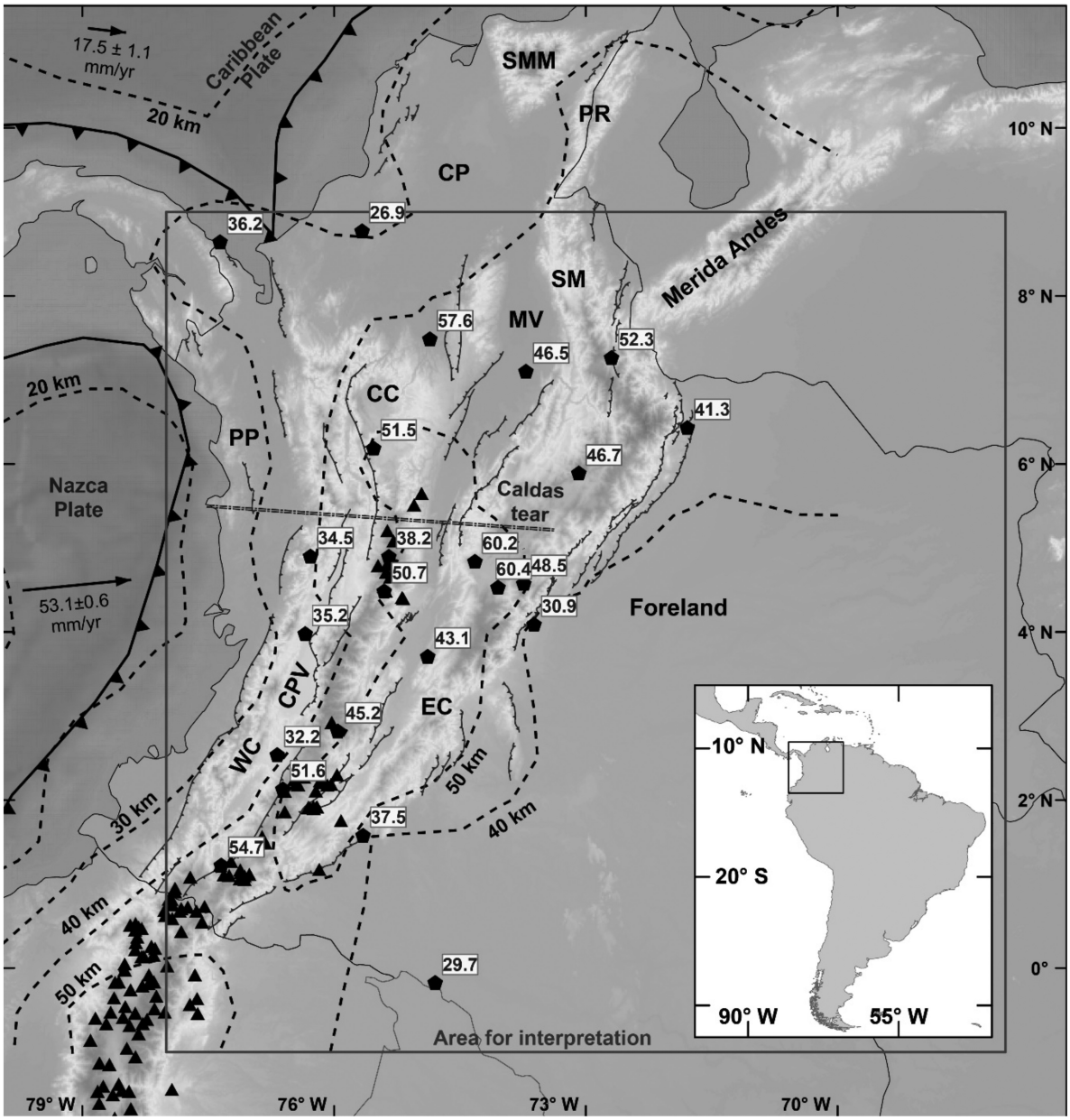

Figure 1. Map of the Colombian Andes showing active thrust faults (Veloza *et al.* 2012), active volcanism (triangles) and the area for interpretation of the gravity inversion. Pentagons depict mean Moho depth (in km) at individual stations from receiver functions (Poveda *et al.* 2015), whereas dashed lines are crustal thickness contours (Poveda *et al.* 2018). Geomorphic features are Magdalena Valley (MV), Cauca-Patía Valley (CPV), Caribbean plains (CP), Santa Marta Massif (SMM), Santander Massif (SM) and Pacific plains (PP). Oceanic plate convergence vectors and rates are relative to stable South America (Mora-Páez *et al.* 2019). The location of the Caldas tear is taken from Vargas (2020).

two layers with different densities. A relative height of the undulating surface (Moho) is calculated with respect to a reference average depth (z_0) and a constant density contrast ($\rho = \rho_{\mathrm{ml}} - \rho_{\mathrm{c}}$) across z_0. The density contrast is defined as the difference between the density of the lithospheric mantle (ρ_{ml}) and the overlying crust (ρ_{c}). The original equation is expressed as:

$$F[\Delta g] = -2\pi G\rho \exp\left(-\left|\vec{k}\right| z_0\right) \sum_{n=1}^{\infty} \frac{\vec{k}^{n-1}}{n!} F\left[h(\vec{r})^n\right], \quad (1)$$

where G is the gravitational constant, $\vec{k}$ is the wavenumber vector and $h(\vec{r})$ is the relative-height vector with respect to z_0. Gao & Sun (2019) re-derived the Fourier transform of eq. (1) allowing the z-axis to be positive downwards, obtaining the following expression that describes the undulations at the interface (Moho):

$$F[-h(\vec{r})] = \frac{F[\Delta g] \exp\left(\left|\vec{k}\right| z_0\right)}{2\pi G\rho} - \sum_{n=2}^{\infty} \frac{\vec{k}^{n-1}}{n!} F\left[(-h(\vec{r}))^n\right]. \quad (2)$$

The inversion procedure is based on an iterative process that uses gravity data (Bouguer anomaly) and constant parameters z_0 and ρ until a convergence condition is reached (Oldenburg 1974). As mentioned by Oldenburg (1974) and Gómez-Ortiz & Agarwal (2005), eq. (2) can be unstable for high frequencies so a high-cut filter multiplying the right-hand side of the equation is applied for

Downloaded from https://academic.oup.com/gji/article/229/3/1964/6521443 by Geoforschungszentrum Potsdam user on 18 May 2022

convergence. The low-pass filter rejects all frequencies above a higher threshold value referred to as SH, accepts all frequencies up to a low value referred to as WH, and applies a cosine filter over frequencies between these two reference values (Oldenburg 1974).

3.1.2 Gravity data and inverted area

Gravity was obtained from two satellite-derived data sets: EGM2008 with an average 2.5 arcmin resolution (Pavlis *et al.* 2012), and EIGEN-6C4 (Förste *et al.* 2014; Ince *et al.* 2019) with an equivalent ∼18 km topographic wavelength from the spherical harmonic solution up to a degree and order of 2190 (e.g. Förste *et al.* 2014; Gómez-García *et al.* 2021). Moreover, a regional total Bouguer anomaly map built by the National Hydrocarbon Agency of Colombia (ANH in Spanish abbreviation), published as a 5 mGal contour map (Graterol & Vargas 2010), was also considered. The latter data set will be hereafter referred to as ANH2010 for simplicity.

In the cases of EGM2008 and EIGEN-6C4, the gridded data were downloaded as available Bouguer gravity anomaly from the International Centre for Global Earth Models (ICGEM; Ince *et al.* 2019), for which details about equations and parameters were used to compute the Bouguer anomaly are given in Barthelmes (2009). A 0.5° grid spacing was used in all data sets given the intended comparison with respect to global Moho models: CRUST1.0 with a resolution of 1° (Laske *et al.* 2013) and GEMMA with a resolution of 0.5° (Reguzzoni & Sampietro 2015). These global models were chosen to aim at a comparison with respect to seismic- and gravity-derived estimations.

The inverted area lies between 79.5–66.5°W and 2.5°S–10.5°N, according to the spatial extent of the ANH2010 data set. However, considering the edge effects, the implemented code uses a cosine taper window for which we applied the suggested truncation window of 10 per cent of the extended data length (Gómez-Ortiz & Agarwal 2005). We choose to keep our Moho depth discussions in the region between 78–68°W and 1°S–9°N (area for interpretation box in Fig. 1), allowing an area for interpretation not closer than 1.5° from the margins of the input gravity data.

As a limitation of our approach, steep Moho changes using this method can be partly evaluated by modifying the grid spacing of the input gravity data. Diminishing the grid spacing allows more constraints (nodes) per unit area which influences the algorithm to invoke steeper transitions in Moho depth. We evaluate this by using different grid spacing (0.2° and 0.25°) before our final 0.5° grid selection. We did not include this analysis in the paper, since the results were more complex and the steep Moho transitions beneath the northwestern Andes were out of the scope of this work. We wanted to depict, therefore, first-order Moho depth distribution and we considered that transitions between different tectono-geologic domains require a more appropriate and detailed methodology than the one used in this work.

3.1.3 The average depth parameter

When using the present approach, gravity inversion has been proven to be strongly influenced by the average depth parameter (z_0) (e.g. Oldenburg 1974; van der Meijde *et al.* 2013; Ydri *et al.* 2020). Because this input parameter (average Moho depth) is a constant value that integrates the whole modelled area, what is recommended is to use the average depth beneath the region, although it might have thicker or thinner parts. The adjustments of thicker and thinner regions are what the inversion process allows to estimate. Therefore, initializing the algorithm with an average depth rather than a depth that might be biased for a particular region of the orogen is a valid approach.

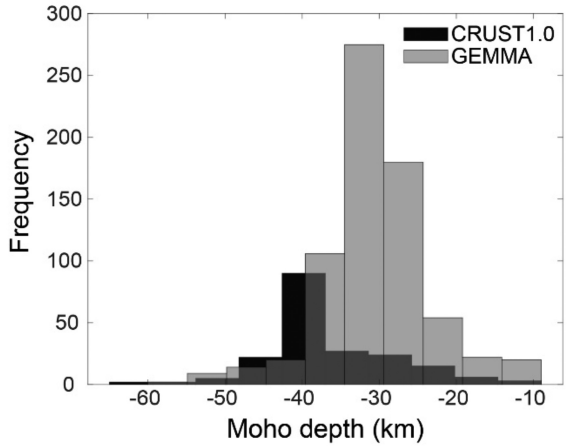

Figure 2. Histograms of Moho depth values derived from global models. From these histograms, we selected reasonable average depth values of 41 and 31 km for comparing the inversions to CRUST1.0 and GEMMA Moho models, respectively.

To select a value of z_0 that allows a proper comparison with the global Moho models, we analyse the depth distribution of CRUST1.0 and GEMMA models within the inverted area (Fig. 2). The associated depth histograms for each model suggest that an average depth of 41 km is a reasonable value to compare with CRUST1.0, whereas a 31 km average depth is well suited to compare with GEMMA. The selection of different starting values, when compared to global models, is justified by the fact that within the target region CRUST1.0 and GEMMA models have substantial differences, CRUST1.0 consistently suggesting thicker crust estimates than GEMMA. For the comparison, we made the *a priori* assumption that one of those models should be more accurate than the other, without knowing which one. By doing this, we selected the data set that minimized the differences with both global models, which means, regardless of which of the global models is more accurate, the chosen data set for final inversion will be better for the studied area than the other data set possibilities.

The comparison between the inverted gravity Moho and the seismic constraints was conducted by converting available crustal thickness into Moho depth (referred to as the depth with respect to mean sea level) below 24 seismic stations (Poveda *et al.* 2015). The conversion was done via subtracting the surface elevation from the crustal thickness at each station (e.g. van der Meijde *et al.* 2013), using the elevation data from the ETOPO1 model (Amante & Eakins 2009). The work of Poveda *et al.* (2015) was considered for such comparison as it contains the best coverage to date along the Colombian region and discusses a comparison between their results and previous gravity and seismic estimates.

To evaluate the convergence of the algorithm, and to select the best parameter combination that minimizes the residual gravity (modelled minus observed data), 5400 different set-ups (combinations of parameter values) were inverted using each gravity data set. The number of different set-ups resulted from allowing the density contrast (ρ) to vary between 0.25–0.60 g cm^3 (Sjöberg & Bagherbandi 2011) with increments of 0.01 g cm^{-3}, whereas the WH and SH frequencies were taken between 0.005–0.0095 and 0.010–0.017 km^{-1} respectively, with increments of 0.0005 km^{-1}.

Downloaded from https://academic.oup.com/gji/article/229/3/1964/6521443 by Geoforschungszentrum Potsdam user on 18 May 2022

The lower bound of 0.005 km^{-1}, representing a wavelength of 200 km, was initially considered after van der Meijde *et al.* (2013), but the effects of lowering this bound will be discussed when improving the final inversion. For simplicity, we will discuss residual gravity in terms of its mean value and associated standard deviation.

3.1.4 Sedimentary basin correction

The applied frequency filter during the inversion allows the removal of short-wavelength sedimentary signals. Yet, the magnitude of the induced mismatch between the inverted Moho depth and the seismic constraints, when not removing the contribution of sedimentary basins with larger wavelength signals, remains debatable when applying this method (e.g. van der Meijde *et al.* 2013 and reference therein). We consider that sedimentary correction is applicable in areas where basement depth and density variation of the sedimentary units are well constrained (e.g. Gómez-Ortiz *et al.* 2005); otherwise, basement signals can be removed leading to Moho depth miscalculations.

Considering the complex deformational pattern, together with a strong variation of lateral thickness and sedimentary facies along the EC and the foreland region, where the major sedimentary basins of Colombia have been reported (Bayona *et al.* 2008; Mora *et al.* 2013; Sarmiento-Rojas 2019; Horton *et al.* 2020), there is a high risk of removing basement gravity signals if the correction is applied. Therefore, we decided not to use this correction before inverting the gravity data and removing short-wavelength sedimentary signals by the applied filter, but being cautious when evaluating the possibility of an overestimated Moho depth in areas where thick sedimentary basins have been proven to exist (e.g. Tirel *et al.* 2004; Aitken *et al.* 2013), such as the Eastern Cordillera, the foreland region and the coastal plains (Fig. 1).

3.2 Choosing the best data set

3.2.1 Comparison between data sets and global models

For comparison between data sets, using inverted depths at nodes in the considered 0.5° grid within the area for interpretation shown in Fig. 1, we focus on the obtained differences in mean residual gravity and standard deviation. Mean residual gravity is somehow similar for all data sets: ANH2010 ranges between −5 and 7 mGal, whereas EGM2008 and EIGEN-6C4 between −1 and 6 mGal, when using both average depths of 41 and 31 km, respectively (Fig. 3). The differences between the data sets were more evident in the standard deviation. When considering a z_0 of 41 km, 529 set-ups showed a standard deviation less than 10 mGal using ANH2010, whereas the minimum standard deviation achieved by EGM2008 and EIGEN-6C4 was between ∼18–19 mGal (Fig. 3a). Similarly, when using a z_0 of 31 km, 1577 set-ups showed a standard deviation less than 10 mGal using ANH2010 data, whereas the minimum standard deviation obtained from EGM2008 and EIGEN-6C4 was ∼14 mGal (Fig. 3b).

When analysing the inversions, by using both average depths, we observed that a higher number of set-ups with lower gravity residuals and standard deviation were accomplished when using a shallower average depth of 31 km, particularly with data from the EIGEN-6C4 model. However, under both scenarios, using a 41 or 31 km average depth, only the ANH2010 data provided inversions with a low gravity residual (−5 to 7 mGal) associated with a standard deviation lower than 10 mGal (Fig. 3). Fig. 3 illustrates the flexibility of the ANH2010 data set to yield inversion models with the lowest gravity residual and standard deviation for a wider range of parameter combinations during the inversion. In simple words, this test shows that the best trade-off between convergence and fitness of the applied algorithm is obtained when using the ANH2010 data set.

Aiming for comparison with global Moho models CRUST1.0 and GEMMA, Moho depth was obtained from each gravity data set by using the parameter combination that minimizes the residual gravity (Supporting Information Table S1). Since the data sets used for inversions are of higher spatial resolution in reference to the global models, the comparison can be made in order to detect first-order differences at a regional scale. In Fig. 4, we show the differences in map view. It can be seen from all data sets, a good agreement for the foreland region, whereas the highest mismatches occur along the cordilleras and coastal plains (darker symbols in Fig. 4).

Regarding CRUST1.0, all data sets show shallower values (squares in Fig. 4), mainly in the central CC and EC and deeper values (circles in Fig. 4) in the northern CC, EC and both the Caribbean and Pacific plains (Figs 4a–c). The largest differences are suggested by the satellite-derived data sets in the Santander Massif and the southern cordilleran belt (darker circles in Figs 4b and c, see also Fig. 1).

Given the higher spatial resolution of GEMMA, the shallower values concerning the global model along the cordilleras (squares) are better depicted; the largest differences are shown by the satellite-derived data sets in central and southern CC and EC (darker squares in Figs 4d–f). Deeper values (darker circles) are mainly shown in northern CC, EC and coastal plains.

EGM2008 and EIGEN-6C4 suggest larger differences along the central-southern cordilleran belt (darker circles in Figs 4e and f). Major differences between data sets and global models, especially for the ANH2010, are within the coastal plains, which might be linked to sedimentary basin infill and uncertainties in the continental to oceanic crust transition (e.g. Gómez-García *et al.* 2021).

Histograms depicting the differences between each inversion and global model are shown in Fig. 5. The inversion with ANH2010 shows that most of the data differ by ±5 km when comparing with global models, whereas the inversions with EGM2008 and EIGEN-6C4 show that most of the data differ with respect to global models by about ±10 km (Fig. 5). Moho depth differences concerning the CRUST1.0 model include, for ANH2010 up to ∼15 km shallower and ∼23 km deeper values (Fig. 5a), for EGM2008 up to ∼20 km shallower and ∼40 km deeper estimates (Fig. 5b), and for EIGEN-6C4 up to ∼20 km shallower and ∼42 km deeper Moho depths (Fig. 5c). The distribution of these differences is bimodal in all data sets, with major peaks at ±5 km for ANH2010 and ±10 km for satellite-derived data sets (EGM2008 and EIGEN-6C4), as well as a second peak depicting 10–17 km deeper values from ANH2010 data, and 10–20 km deeper estimates from satellite-derived inversions (EGM2008 and EIGEN-6C4; Fig. 5).

Regarding the GEMMA model, differences are up to ∼20 km shallower and ∼15 km deeper values for ANH2010 data (Fig. 5d), up to ∼40 km shallower and ∼25 km deeper estimates for EGM2008 (Fig. 5e), and up to ∼32 km shallower and ∼20 km deeper Moho depths for EIGEN-6C4 data (Fig. 5f). Those differences depict a normal distribution in all data sets, with a mean of 0.49 km and a variance of 27.56 km for ANH2010, a mean of 0.31 km, and a large variance of 52.51 km for EGM2008, and a mean of 0.31 km and a variance of 43.30 km for EIGEN-6C4 (Fig. 5). Correlation coefficients, when compared to CRUST1.0 and GEMMA models

Downloaded from https://academic.oup.com/gji/article/229/3/1964/6521443 by Geoforschungszentrum Potsdam user on 18 May 2022

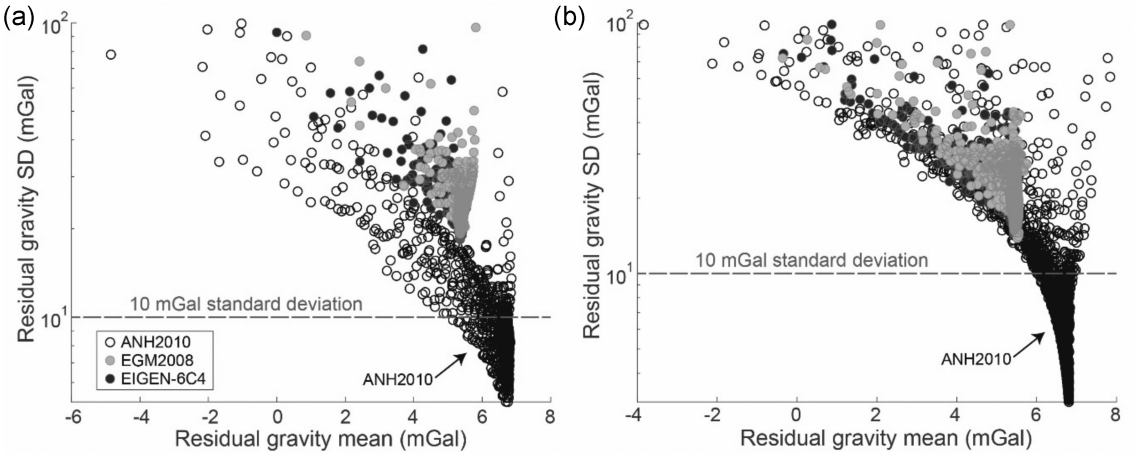

Figure 3. Mean residual gravity and standard deviation (SD) for the different gravity data sets, varying ρ, WH and SH parameters. (a) Using an average depth of 41 km. (b) Using an average depth of 31 km. Only set-ups with a standard deviation lower than 100 mGal were plotted.

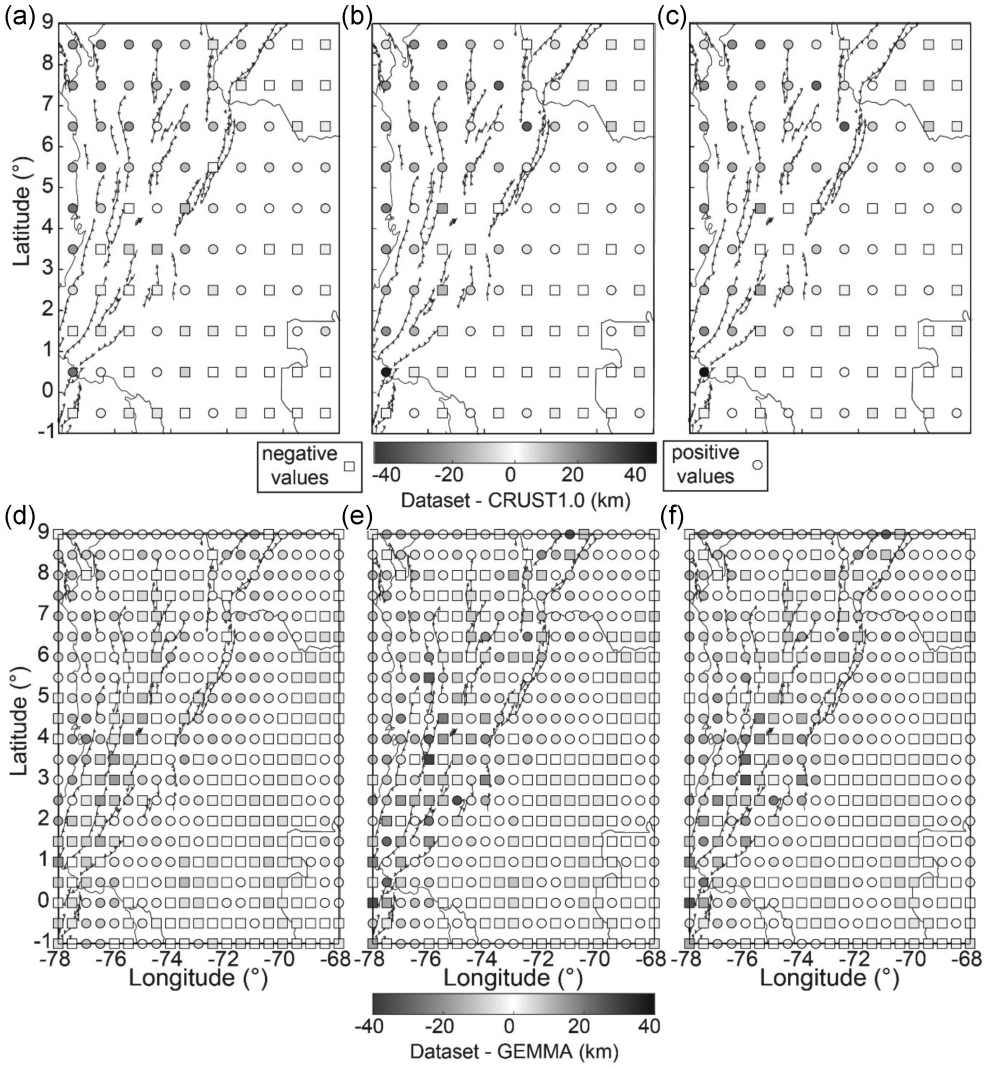

Figure 4. Moho depth differences between inversion of data sets and global models using a 41 km average depth: (a) ANH2010 minus CRUST1.0; (b) EGM2008 minus CRUST1.0; (c) EIGEN-6C4 minus CRUST1.0. Using a 31 km average depth: (d) ANH2010 minus GEMMA; (e) EGM2008 minus GEMMA; (f) EIGEN-6C4 minus GEMMA. Extension of the area for comparison as depicted by the area for interpretation box in Fig. 1. Negative values are shown as squares and positive ones as circles. Active thrust faults as in Fig. 1.

Downloaded from https://academic.oup.com/gji/article/229/3/1964/6521443 by Geoforschungszentrum Potsdam user on 18 May 2022

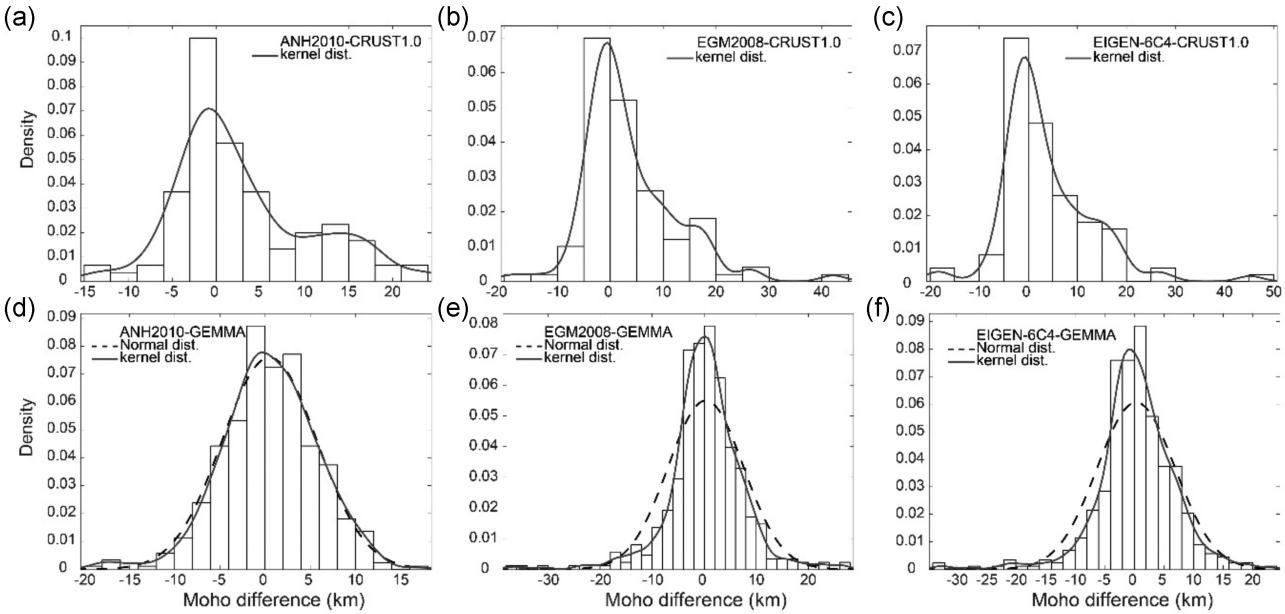

Figure 5. Histograms with kernel density estimates and normal density distributions show the differences between inverted gravity Moho and global Moho depth models. (a–c) Data sets minus CRUST1.0 model. (d–f) Data sets minus GEMMA model. A higher number of bins for GEMMA is shown given its higher spatial resolution (see Fig. 4).

respectively, are 0.27 and 0.52 for ANH2010, 0.24 and 0.36 for EGM2008, and 0.25 and 0.40 for EIGEN-6C4 inversion.

3.2.2 Consistency with receiver functions estimates

To evaluate the consistency of the Moho inversions from the gravity data sets with respect to seismic constraints (Poveda *et al.* 2015), we analyse the Moho depth distribution beneath the northwestern Andean region. The inversions resulting from all data sets, using an average depth of 41 km and associated parameters (Supporting Information Table S1), show a prevalent Moho depth of 40–50 km, with shallower 30–40 km values in the southern foreland region, beneath WC and southeast of the Merida Andes, and a deeper 50–60 km expression beneath the EC with the deepest anomaly around 1°S–2°N (Figs 6a–c, see also Fig. 1 for geographical locations). Conversely, the inversion with a shallower average depth of 31 km, shows a dominant 30–40 km gravity Moho depth in all data sets (Figs 6d–f). As expected, by using a lower average depth, the inversion resulted in a regional-scale shallower Moho (e.g. Ydri *et al.* 2020), which strongly differs from available receiver functions estimates (see Fig. 1 for seismic depth estimates).

Because of the better agreement between the inverted Moho depth and seismic constraints, while using the 41 km average depth (Figs 1 and 6), we use these inversions to compare with depth values derived from receiver functions. For such comparison, we interpolate the inverted Moho depth at the location of individual stations reported by Poveda *et al.* (2015). An uncertainty of ±4 km is suggested for the inverted gravity values, obtained from a variation in the average depth parameter by ±2 km (e.g. van der Meijde *et al.* 2013).

For simplicity, given that seismic constraints are reported in the form '$A \pm B$ *km*', we will refer to the depth '$A - B$ *km*' as the lower (shallower) seismic bound and '$A + B$ *km*' as the upper (deeper) seismic bound. Furthermore, because we refer to the seismic station's abbreviation (e.g. ROSC), we provide a geographical location (e.g. central EC), although the stations are depicted in Fig. 7.

In this regard, shallower values (squares in Fig. 7) were suggested by the inversion with ANH2010 data for two stations, with a mismatch in-depth above 4 km (uncertainty) regarding the lower seismic bounds (Supporting Information Table S1). Those stations are ROSC (central EC) and ZAR (transition from CC to the Caribbean plains), where differences between the maximum estimate (inverted depth plus 4 km) and the lower seismic bound, are ∼0.5 and ∼10.8 km, respectively (Fig. 7a, Supporting Information Table S1). EGM2008 and EIGEN-6C4 suggest for seven stations, shallower values with a mismatch in-depth above 4 km compared with the lower seismic bounds. The differences between the maximum estimate (inverted depth plus 4 km) and lower seismic bound, range 2.6–10.6 km at ANIL, HEL and ZAR stations (northern CC and transition to Caribbean plains), between 1.2 and 11.8 km at BOCO, ROSC and RUS (central-northern EC), and <1 km at PAM station (Santander Massif; Figs 7b and c, Supporting Information Table S1).

In terms of deeper estimates (circles in Fig. 7), the inversion with ANH2010 data suggests, for eight stations, greater Moho depths with a mismatch above 4 km (uncertainty) compared with the upper seismic bounds (Fig. 7a, Supporting Information Table S1). Differences between the minimum estimate (inverted depth minus 4 km) and upper seismic bound, range 0.2–9 km at CAP2 and MON stations in the Caribbean plains, station PAL on the Western Cordillera, stations POP2 and RREF along the Central Cordillera, station PRA and VIL along the Eastern Cordillera, and station PTLC within the foreland region (Fig. 7a). Inversions from EGM2008 and EIGEN-6C4 suggest deeper estimates with depth mismatching above 4 km at six stations (Figs 7b and c), including, MON station in the Caribbean plains, station YOT at the Western Cordillera, stations PCON, POP2 and RREF along the Central Cordillera, and station VIL on the Eastern Cordillera. Differences between the minimum estimate (inversion depth minus 4 km) and the upper seismic bound, range between 2.9 and 12.7 km at the mentioned stations for inverted satellite-derived data sets (Supporting Information Table S1). The largest mismatch between the data sets and the upper seismic bound

Downloaded from https://academic.oup.com/gji/article/229/3/1964/6521443 by Geoforschungszentrum Potsdam user on 18 May 2022

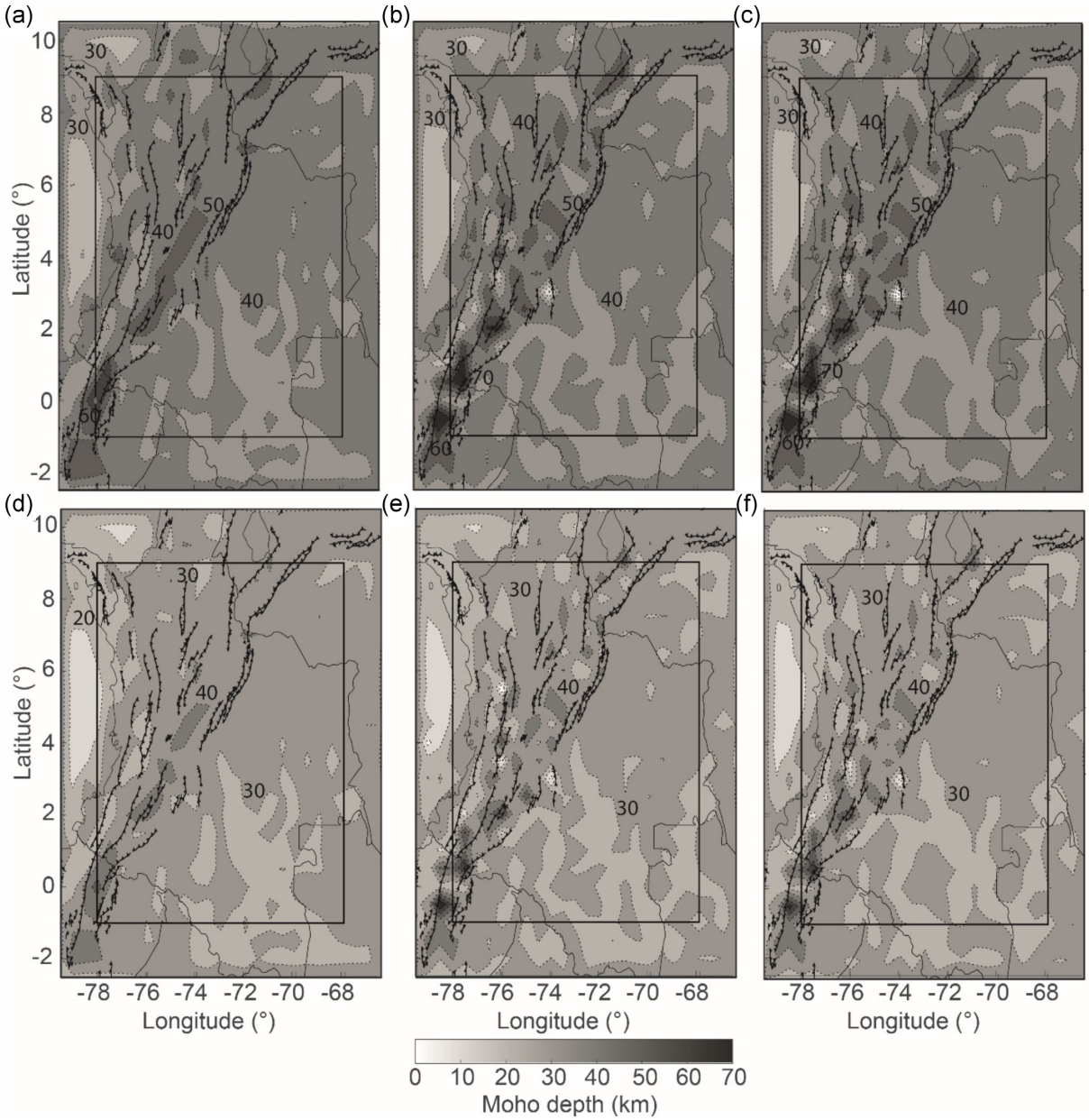

Figure 6. Inversion using a z_0 of 41 km, from different data sets: (a) ANH2010; (b) EGM2008; (c) EIGEN-6C4. Inversion using a z_0 of 31 km: (d) ANH2010; (e) EGM2008; (f) EIGEN-6C4. Active thrust faults as in Fig. 1. The black box depicts the area for interpretation shown in Fig. 1. A smooth interpolation was not applied at this stage. When reducing the average depth parameter from 41 to 31 km, a regional shallower Moho depth inversion is obtained.

are depicted at VIL station (eastern foothills of EC), yielding differences of ∼9 km using the ANH2010 inversion, and between 11.6 and 12.7 km in the inversion from satellite-derived data sets (darker circles in Fig. 7). A correlation coefficient between the inverted values and the mean seismic depths yields 0.60 for ANH2010, 0.16 for EGM2008 and 0.17 for EIGEN-6C4 (Supporting Information Table S1).

In summary, the ANH2010 inversion results in a higher number of matching stations in terms of Moho depth, in fewer stations differing in more than 4 km in depth with respect to seismic bounds, and in a higher correlation coefficient when compared to mean seismic estimations (Fig. 7). The latter, coupled with the ability shown by this data set to achieve a higher number of set-ups with low residual gravity and standard deviation lower than 10 mGal (Fig. 3), reflects its potential to be used for the northwestern Andes and surroundings. Therefore, we choose this data set to obtain the final Moho inversion.

4 RESULTS: IMPROVED INVERSION AND OVERVIEW OF THE NORTHWESTERN ANDEAN MOHO TOPOGRAPHY

To improve the ANH2010 inversion, we further investigated the parameter values that minimize the differences with seismic constraints while yielding a standard deviation <10 mGal (minimizing residual gravity). For this, the WH range was incremented (0.001–0.0095 km^{-1}) to filter lower frequencies for evaluating the sensi-

Downloaded from https://academic.oup.com/gji/article/229/3/1964/6521443 by Geoforschungszentrum Potsdam user on 18 May 2022

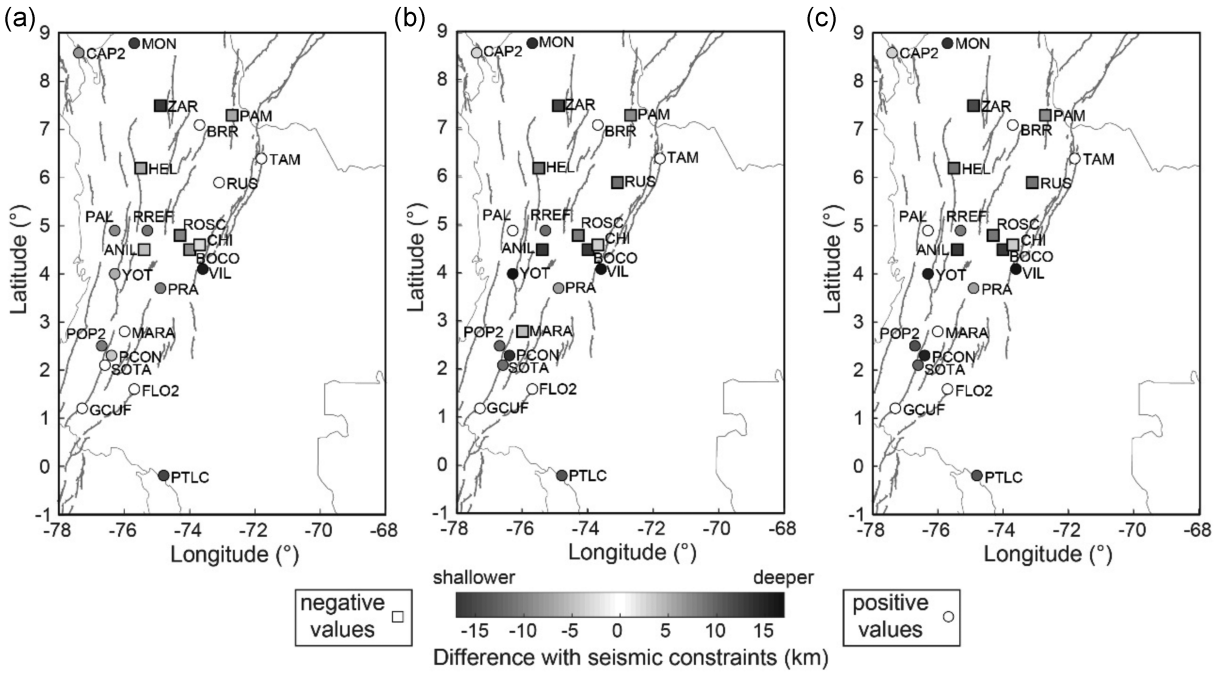

Figure 7. Depth comparison between inverted Moho and seismic constraints when using a 41 km average depth: (a) ANH2010; (b) EGM2008; (c) EIGEN-6C4. Zero represents inverted values in the range of seismic constraints, shallower values (negative) are represented by squares and deeper values (positive) are represented by circles (see also Supporting Information Table S1).

tivity of deeper sources. Furthermore, the average depth parameter was varied between 31 and 41 km with a 0.25 km step increment. The best combination of parameters minimizing the differences regarding mean Moho depth values from receiver functions was: an average depth of 37 km, a density contrast of 0.35 g cm^{-3}, and lower (WH) and upper (SH) cut-off frequencies of 0.001 and 0.0155 km^{-1}, respectively. The improved Moho inversion is shown in Fig. 8 depicting a broad depth distribution for which uncertainty of ±4 km is also considered as previously mentioned. It is worth noting that expanding the range of the lower cut-off frequency increased the agreement with respect to seismic constraints and allowed using a lower density contrast for the inversion.

This set-up yields a mean residual gravity of 6.7 mGal and a standard deviation of 9.9 mGal, with a correlation coefficient with respect to mean seismic values of 0.63 (Supporting Information Table S1). In a broad view, the inverted Moho depicts a 40–50 km depth beneath the cordilleran belt reaching depths beyond 50 km below the Eastern Cordillera, and shallower depths between 30–40 km mainly along the foreland region, the Western Cordillera and the coastal plains (Fig. 8a). Within the foreland region, residual gravity shows small patches up to 10 mGal where shallow anomalies are also depicted (<30 km), which are considered inversion artefacts; the rest of the foreland region agrees with a Moho between 30–40 km, although a deeper expression (>40 km) is shown in the northwesternmost foreland and the northeastern foothills of the EC (Fig. 8a). Small anomalies of 40 km depth in the inner foreland are also considered inversion artefacts. The obtained 30–40 km Moho depth beneath the foreland region agrees well with the ∼35 km depth (Fig. 9) obtained by Uieda & Barbosa (2017) from gravity inversion using the spherical harmonic model GOCO5S but considering a more complex inversion approach.

Beneath the Central and Eastern cordilleras, the Santander Massif and the Merida Andes (see Fig. 1), the gravity Moho shows a 40–60 km depth (Fig. 8a). Higher values between 50 and 60 km are shown beneath the EC trend in an irregular pattern between 2°N and 6°N, and a deeper expression (>60 km) is depicted at a southern position below the modern magmatic arc (1°S–1°N). Within the EC and the Santander Massif, residual gravity shows only small patches of 10 mGal and up to 20 mGal in the southern cordilleran belt, arguing in favour of some degree of volcano-sedimentary basin residual gravity to the south. For the northern and central Eastern Cordillera (TAM, RUS, ROSC, CHI, BOCO stations) the gravity Moho (40.5–53.8 km) agrees well with seismic constraints (34.9–69.0 km), although for stations PRA and VIL the inversion suggests deeper values (Fig. 8c; Supporting Information Table S1). For the Santander Massif, seismic constraints at the PAM station suggest a 48.1–56.5 km Moho depth, for which the gravity inversion agrees well, yielding 45.3 ± 4 km. Our inversion differs in this part of the orogen with respect to the estimates presented by Uieda & Barbosa (2017; Fig. 9) mainly because as they discussed, their method does not fully recover deeper Moho expressions within the Andean region.

In the CC, a Moho depth between 40–50 km is shown with a positive residual gravity around 10 mGal. Beneath the RREF station (see Fig. 8c), located at ∼4.6°N at the Nevado del Ruiz active volcano, the suggested gravity Moho depth yields 45.3 ± 4 km which is slightly deeper than the depth suggested by seismic constraints (37.1–39.3 km). However, the Moho determination beneath this station is of higher complexity than that at ANIL station at the Cerro Machín volcano (see Fig. 8c), which in fact, yields a Moho depth between 47.4–54.1 km being located ∼60 km to the south of RREF station. At the RREF station, the compiled receiver functions show a larger azimuthal variation in delay times for the Moho determination, which implies a non-simple crust–mantle transition allowing a wider expression of the *P* to *s* converted phase arrival in the receiver functions, and thus, a higher uncertainty in the reported Moho depth. Higher delay times for the RREF station are observed for backazimuths between 153° and 282°, whereas at ANIL station

Downloaded from https://academic.oup.com/gji/article/229/3/1964/6521443 by Geoforschungszentrum Potsdam user on 18 May 2022

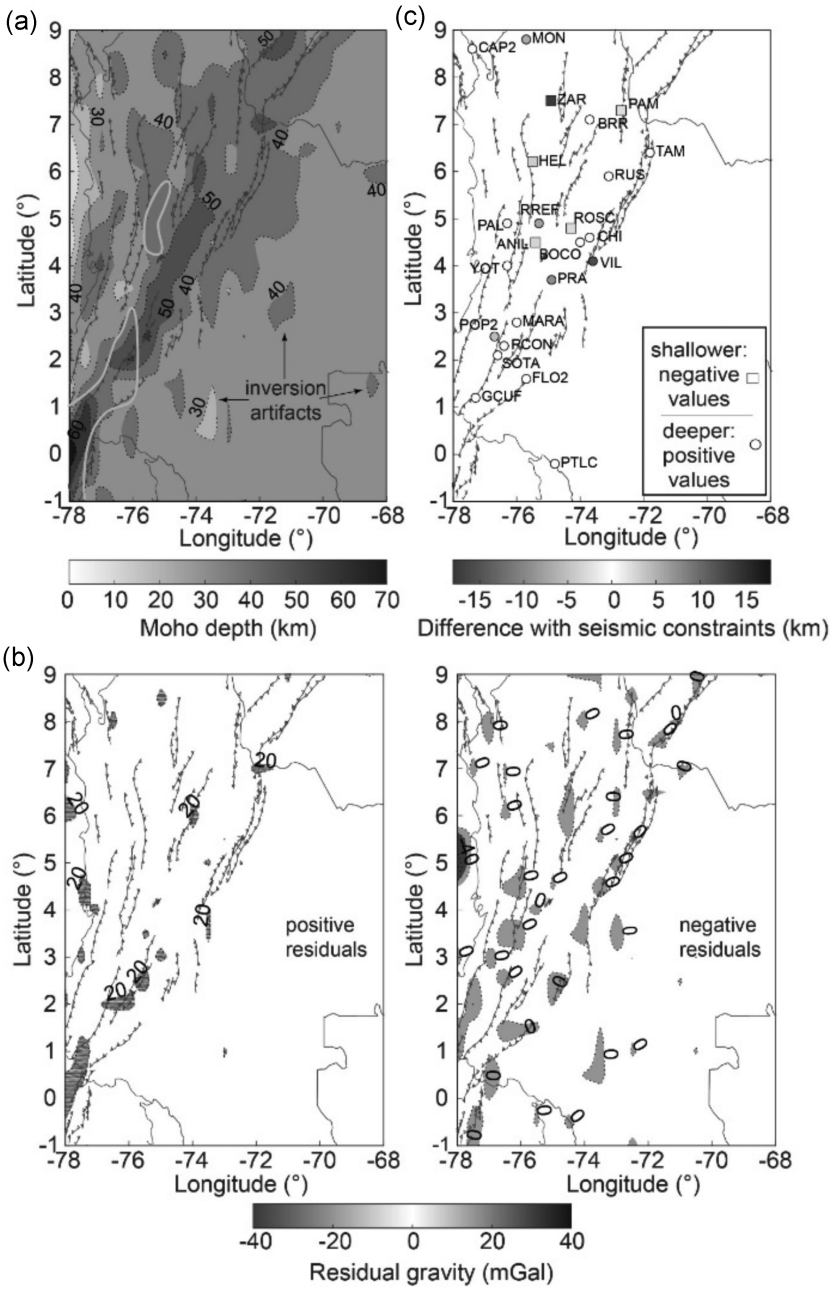

Figure 8. Results of gravity inversion after selecting the best set-up for the ANH2010 data set (see Supporting Information Table S1). (a) Gravity Moho depth with dotted contours. Regions of active volcanism are represented by white thick solid polygons (see also Fig. 1). (b) Gravity residual associated with the inversion. (c) Inverted depth compared with respect to seismic constraints (Poveda *et al.* 2015). Thrust faults in all panels as in Fig. 1.

the delay time for the converted phase (Ps) is better constrained, and therefore the Moho depth provides a lower uncertainty (Poveda 2013). At ANIL station our inversion suggests 44.2 ± 4 km, which together with the previous value at RREF station, correlates well with seismic constraints.

For the southern CC, seismic estimates argue in favour of a 40.3–57.1 km Moho depth beneath MARA, PCON and SOTA stations, which are similar to values of 47.7–51.5 km estimated at those sites from our inversion (Fig. 8c). The deepest Moho (>60 km) lies in a southern latitude beneath the Central Cordillera (1°S–1°N), suggesting a spatial correspondence with the central-southern volcanic segment (Fig. 8a). At station GCUF, our inversion suggests 51.6 ± 4 km depth, matching the seismic constraints that indicate 54.7 ± 8.2 km Moho depth. The CC claims a thinner crust compared to the EC; our inversion agrees well, in that sense, with the estimations presented by Uieda & Barbosa (2017), although they present slightly shallower values beneath the northernmost Central Cordillera (Fig. 9).

Along the Western Cordillera, where residual gravity yields 0–10 mGal, a 30–40 km gravity Moho depth is estimated, which agrees well with seismic constraints, arguing a 31–40 km depth (Monsalve *et al.* 2013; Poveda *et al.* 2015). A deeper Moho (>40 km) is depicted beneath the Pacific plains between 3°N and 5°N; the nature of this anomaly is not well understood but it might be reflecting an overestimated depth caused by the overlooked effect of a thick sedimentary infill (Case *et al.* 1971). Hence, the Moho in this anomalous

Downloaded from https://academic.oup.com/gji/article/229/3/1964/6521443 by Geoforschungszentrum Potsdam user on 18 May 2022

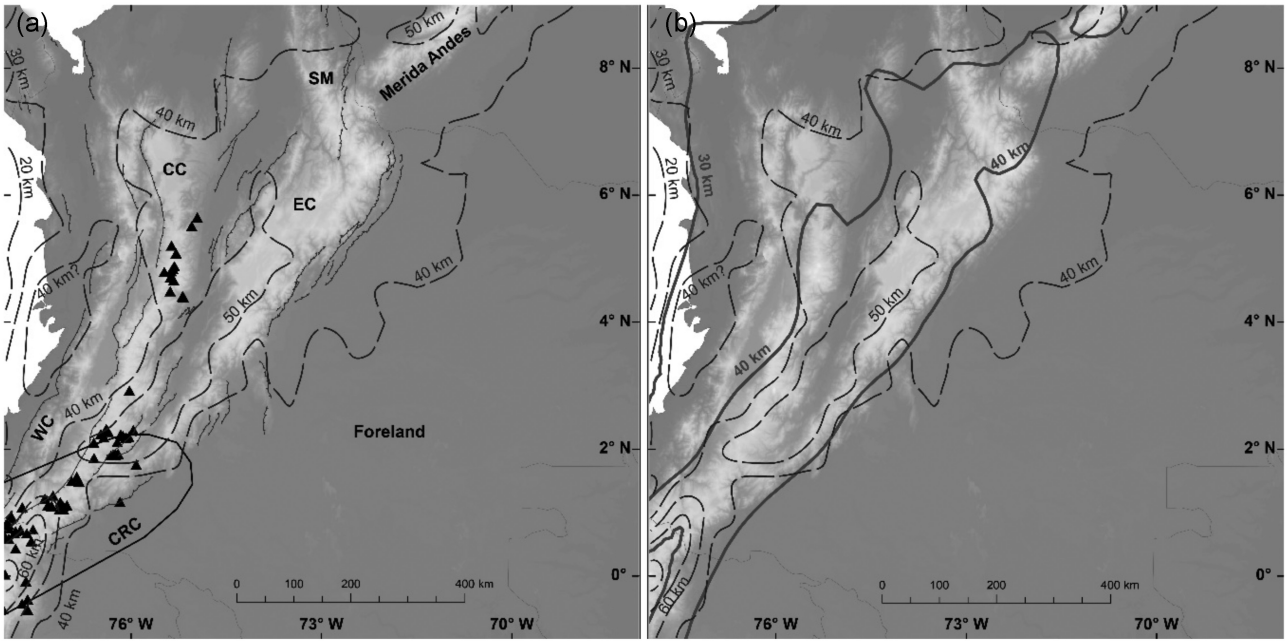

Figure 9. (a) Suggested Moho distribution beneath the northwestern Andes and foreland region not showing contours of inversion artefacts and likely overestimations in some regions. The thick expression in the Pacific region enclosed by the 40 km contour with a question mark (40 km?) might reflect an overestimated Moho due to sedimentary infill. Black triangles are active volcanoes, CRC stands for Carnegie ridge continuation (Gutscher *et al.* 1999) and thrust faults are presented as in Fig. 1. (b) Comparison between regional-scale Moho depth estimates: dashed lines are depths obtained by our inversion, whereas solid thick lines are from Uieda & Barbosa (2017).

region could be shallower than suggested from our inversion. Except for such presumable overestimation, a general agreement with the Moho depths estimated by Uieda & Barbosa (2017) is achieved (Fig. 9).

Seismic estimations in the Caribbean plains claim 23.2–30.6 km Moho depth at MON station, whereas gravity inversion suggests a slightly deeper Moho of 35.9 ± 4 km. The latter may reflect the contribution of sedimentary units to some degree, which in fact, have been constrained in the order of 4–6 km-thick in several parts of this region (Bernal-Olaya *et al.* 2015; Poveda *et al.* 2018). However, as shown in Fig. 8(a), the Caribbean plains show a broad 30–40 km Moho depth which is in good agreement with estimations based on integrated seismic and gravity data (Bernal-Olaya *et al.* 2015). In this region though, a large mismatch at ZAR station is obtained: while seismic constraints suggest a depth of 57.6 ± 2.9 km, our gravity inversion yields 36.7 ± 4 km; taking into account the location of the station within the southern Caribbean plains and to the north of the termination of the high topography of Central Cordillera (see Fig. 1), we consider our inverted value not to be highly mistaken, especially when considering similar values obtained from integrated seismic and gravity data along this region (Bernal-Olaya *et al.* 2015).

5 DISCUSSION

A general tendency of a relatively deep continental Moho beneath the three cordilleras of the northwestern Andes is observed, with higher values beneath the EC and lower values beneath the WC (Fig. 9). A moderately shallow Moho is depicted along the foreland region, while the lowest values were obtained within the coastal plains (Fig. 9). In a broad sense, the inverted Moho shows some consistency with isostatic equilibrium, and although residual topography has been argued within the orogen especially in northern Eastern Cordillera (Yarce *et al.* 2014; Siravo *et al.* 2019), the magnitude of such positive residual topography of less than 2 km lies within our depth uncertainty (± 4 km). Because some influence of sedimentary basins along the coastal plains might be affecting the inversion, overestimating in some degree the Moho depth, our tectonic interpretation will be mostly focused beneath the cordilleran belts.

Several interesting features are shown by the obtained gravity Moho distribution. In a first instance, a deep expression of the Moho (>40 km) in the northwesternmost foreland and the northeastern foothills of the Eastern Cordillera (Fig. 9), is located to the east of the EC in a region where the mountain range is wider, shows its highest elevations, and where a thickened crust, even above 60 km, have been constrained by receiver functions (Poveda *et al.* 2015; Monsalve *et al.* 2019). Under the assumption of a gentle shallowing of the Moho, we consider that the expression of the northwestern foreland can be explained as a direct consequence of the adjacent thickened EC involving the fold and thrust deformation migration from the range towards the foreland, and the flexural deformation constrained in the eastern foothills and adjacent foreland region (Bayona *et al.* 2008; Parra *et al.* 2012; Siravo *et al.* 2018). The wider and thicker expression of the EC in the central-northern part of the cordillera where thick-skin deformation has been constrained (Parra *et al.* 2012; Mora *et al.* 2013; Siravo *et al.* 2018), allows for a higher load which can trigger a flexural deformation in the eastern foothills (see Bayona *et al.* 2008), resulting in a deepening of the Moho beneath the westernmost foreland adjacent to the cordilleran belt, as it has been proposed for the Central Andes (e.g. Whitman 1994).

For the northern and central Eastern Cordillera, the gravity Moho agrees well with seismic constraints, although it suggests deeper values beneath the eastern foothills (Fig. 8c). We consider the deep expression of the Moho beneath this part of the orogen to be related

Downloaded from https://academic.oup.com/gji/article/229/3/1964/6521443 by Geoforschungszentrum Potsdam user on 18 May 2022

to the thickening history of the range, especially during the Cenozoic when thick-skinned deformation took place, as constrained along different segments of the cordillera (Bayona *et al.* 2008; Mora *et al.* 2013; Mora-Páez *et al.* 2016; Saeid *et al.* 2017; Siravo *et al.* 2018). This shortening history is somehow represented in the inversion, by the spatial correspondence between deeper values along the EC and active thrust faults (Fig. 9a). Furthermore, the tectonic shortening resulting in the thickening of the crust will allow higher topographic expressions associated with an isostatic response. This is the case of the Eastern Cordillera, where the highest topographic features are depicted above the thicker crustal regions, as shown by receiver functions (Poveda *et al.* 2015), and although there have been some suggestions of positive residual topography in the range (Yarce *et al.* 2014; Siravo *et al.* 2018), as previously mentioned, the amount of excess in topography (<2 km) is within our inversion uncertainty (± 4 km).

For the central section, a contribution of magmatic underplating has also been interpreted more clearly beneath the RUS station (Fig. 8c; Monsalve *et al.* 2019). We speculate that localized magmatic underplating at the base of the crust in this part of the orogen allows a deeper Moho expression beneath the central part of the EC and shallower depths towards the north of the range and the Santander Massif.

The relationship between the volcanically active segments of the hinterland and the Moho depth is not easy to envision. The northern segment of the modern volcanic arc does not seem to be correlated with a distinctive geometry of the Moho depth. Conversely, the southern portion of the arc lies above the deepest Moho expression within the inverted area (>60 km at 1°S–1°N; Fig. 9). For this region, lower crustal xenoliths brought to the surface by Plio-Pleistocene volcanism, argue for a much thicker crust (up to 80 km) than available seismic constraints and our inversion estimates (e.g. Bloch *et al.* 2017). However, the thickening history of this part of the orogen is still poorly constrained. Poveda *et al.* (2015) discussed high Vp/Vs ratios beneath the volcanic centres, claiming the potential presence of mafic materials at the base of the crust, which might be contributing to its thick structure. Because our approach is not robust enough to discuss in more detail the magmatic underplating hypothesis, we consider it as one of the possibilities to explain the thicker expression at this latitude. On the other hand, Bloch *et al.* (2017), based on depth and density estimations from recovered xenoliths, interpreted a gravitationally unstable lower crust for which they claimed foundering tectonics. Again, our approach is not able to discern between these two feasible mechanisms and are thus, included as possibilities.

Furthermore, we include an extra possibility for thickening this part of the orogen, based on the work presented by Bishop *et al.* (2017) in the Central Andes, where the increase in crustal thickness is associated with the Nazca ridge; this can be a good example to compare with, since it is proposed, for a segment of the Andes associated with a ridge that resembles the Carnegie setting interacting obliquely with the margin. The projection of the subducted part of the Carnegie ridge in our study area (Fig. 9a) allows us to hypothesize that it might be affecting the upper plate structure, particularly along the southern part of the area where our inversion yields a thick crust; yet, little is known about the role of this buoyant entity in the deformation pattern in this part of the orogen. We speculate that the subduction of this element could be causing crustal thinning in the overriding South American plate, localized along the trajectory of the ridge, and prompting local thickening in the surrounding areas by lateral lower crust displacement, as suggested for the central Andes due to the subduction of the Nazca ridge (Bishop *et al.* 2017). As shown in Fig. 1, the thinning of the overriding plate agrees well with receiver functions (Poveda *et al.* 2015, 2018) suggesting a disrupted thickened crust along the Colombian-Ecuador border (see also Koch *et al.* 2021), where the continuation of the Carnegie ridge subduction has been proposed (Gutscher *et al.* 1999). Additionally, xenolithic data claiming a much thicker crust compared to seismic constraints in the Colombian region, coupled with the short-wavelength pattern shown by our inversion in this area, allowed us to favour a local thickening during the advance of the ridge subduction rather than a regional crustal shortening mechanism.

6 CONCLUSIONS

Through a comparison of multiple gravity data sets, the regional airborne Bouguer gravity anomaly map, built by the National Hydrocarbon Agency of Colombia (Graterol & Vargas 2010), was selected as the most suitable data set to gain insights into the Moho depth beneath the northwestern Andes. A general tendency of a Moho depth between 30 and 60 km beneath the three cordilleras in the Colombian Andes is observed, with deep values found beneath the Eastern Cordillera (50–60 km), relatively shallow values beneath the Western Cordillera (30–40 km) and an anomalously deep Moho in the southern cordilleran belt beneath the modern magmatic arc (>60 km). A moderately shallow Moho (30–40 km) is obtained along the foreland region and the coastal plains; in the latter region, some influence of the sedimentary basins is likely causing an overestimation of the Moho depth.

Three main expressions of regional extent were detected in our inversion: (1) a deep expression (>40 km) in the northwesternmost foreland, interpreted as a direct consequence of a gentle shallowing of the Moho from the adjacent thickened Eastern Cordillera involving the fold and thrust deformation migration from the range towards the foreland, and the flexural deformation constrained in the eastern foothills and adjacent foreland region (Bayona *et al.* 2008; Parra *et al.* 2012; Siravo *et al.* 2018), (2) a regional deep expression (50–60 km) along the Eastern Cordillera trend, interpreted as a combination of its shortening history involving multiple Cenozoic thick-skinned deformational events (Bayona *et al.* 2008; Mora *et al.* 2013), and magmatic underplating (Monsalve *et al.* 2019) and (3) a deep anomaly (>60 km) in a southern latitude beneath the modern magmatic arc (1°S–1°N), which can be interpreted as a combined result of the potential presence of mafic materials at the base of the crust (Poveda *et al.* 2015), a gravitationally unstable lower crust experiencing foundering tectonics (Bloch *et al.* 2017) and lateral lower crust displacement triggered by the subducting Carnegie ridge.

ACKNOWLEDGMENTS

We thank G. Posada and L. Ramírez-Hoyos for their help in gathering the ANH data in a useful format, and Thorsten Becker for fruitful discussions, which allowed us to improve the quality of our manuscript. Comments and suggestions from editors B. Vermeersen and F. Storey, as well as those from R. Bernal and two anonymous reviewers substantially improved the quality of this work. DSA-J contributed to this paper in its conceptualization, formal analysis and visualization; led the selection of the methodology to be applied; processed the data; wrote the original draft; and led the writing–review and editing. GM contributed to the conceptualization and formal analysis; supervised the chosen methods; validated results; and led with the first author the writing–review and editing.

Downloaded from https://academic.oup.com/gji/article/229/3/1964/6521443 by Geoforschungszentrum Potsdam user on 18 May 2022

SL contributed to the formal analysis, and writing–review and editing. AMG-G contributed to the visualization, conceptualization, and writing–review and editing. This work was supported by the Fundación para la Promoción de la Investigación y la Tecnología (Project 4.634).

DATA AVAILABILITY

All used data and codes can be obtained from the cited references. In Supporting Information Table S1, the reader can find the parameter values used in the multiple inversions as well as the comparison regarding seismic constraints discussed in this paper.

REFERENCES

Aitken, A.R.A., Salmon, M.L. & Kennett, B.L.N., 2013. Australia's Moho: a test of the usefulness of gravity modelling for the determination of Moho depth, *Tectonophysics,* **609,** 468–479.

Amante, C. & Eakins, B.W., 2009. ETOPO1 1 arc-minute global relief model: procedures, data sources and analysis, NOAA Tech. Memo. NESDIS NGDC-24, 19 pp, https://doi.org/10.1594/PANGAEA.769615.

Barthelmes, F., 2009. Definition of functionals of the geopotential and their calculation from spherical harmonic models: theory and formulas used by the calculation service of the International Centre for Global Earth Models (ICGEM), Dtsch. Geo-ForschungsZentrum GFZ 1–5. https://doi.org/10.2312/GFZ.b103-0902-26.

Bayona, G., Cortés, M., Jaramillo, C., Ojeda, G., Aristizabal, J.J. & Reyes-Harker, A., 2008. An integrated analysis of an orogen-sedimentary basin pair: latest Cretaceous–Cenozoic evolution of the linked Eastern Cordillera orogen and the Llanos foreland basin of Colombia, *Bull. geol. Soc. Am.,* **120,** 1171–1197.

Beck, S.L. & Zandt, G., 2002. The nature of orogenic crust in the central Andes, *J. geophys. Res.,* **107,** ESE 7–1-ESE 7-16.

Bernal-Olaya, R., Mann, P. & Vargas, C.A., 2015. Earthquake, tomographic, seismic reflection, and gravity evidence for a shallowly dipping subduction zone beneath the Caribbean margin of Northwestern Colombia, *AAPG Mem*., **108,** 247–269.

Bishop, B.T., Beck, S.L., Zandt, G., Wagner, L., Long, M., Antonijevic, S.K., Kumar, A. & Tavera, H., 2017. Causes and consequences of flat-slab subduction in southern Peru, *Geosphere,* **13,** 1392–1407.

Blanco, J.F., Vargas, C.A. & Monsalve, G., 2017. Lithospheric thickness estimation beneath Northwestern South America from an *S*-wave receiver function analysis, *Geochem. Geophys. Geosyst.,* **18,** 1376–1387.

Bloch, E., Ibañez-Mejia, M., Murray, K., Vervoort, J. & Müntener, O., 2017. Recent crustal foundering in the Northern Volcanic Zone of the Andean arc: petrological insights from the roots of a modern subduction zone, *Earth planet. Sci. Lett.,* **476,** 47–58.

Cardona, A. *et al.*, 2012. From arc-continent collision to continuous convergence, clues from Paleogene conglomerates along the southern Caribbean–South America plate boundary, *Tectonophysics,* **580,** 58–87.

Cardona, A., León, S., Jaramillo, J.S., Montes, C., Valencia, V., Vanegas, J., Bustamante, C. & Echeverri, S., 2018. The Paleogene arcs of the northern Andes of Colombia and Panama: insights on plate kinematic implications from new and existing geochemical, geochronological and isotopic data, *Tectonophysics,* **749,** 88–103.

Case, J.E., Duran S, L.G., Alfonso, L.R. & Moore, W.R., 1971. Tectonic investigations in western Colombia and eastern Panama, *Bull. geol. Soc. Am.,* **82,** 2685–2712.

Chiarabba, C., De Gori, P., Faccenna, C., Speranza, F., Seccia, D., Dionicio, V. & Prieto, G.A., 2015. Subduction system and flat slab beneath the Eastern Cordillera of Colombia, *Geochem. Geophys. Geosyst.,* **17,** 16–27.

Förste, C. *et al.*, 2014. EIGEN-6C4 The latest combined global gravity field model including GOCE data up to degree and order 2190 of GFZ Potsdam and GRGS Toulouse, *GFZ Data Serv*., https://doi.org/https://doi.org/10.5880/icgem.2015.1.

Gao, X. & Sun, S., 2019. Comment on "3DINVER.M: a MATLAB program to invert the gravity anomaly over a 3D horizontal density interface by Parker-Oldenburg's algorithm", *Comput. Geosci.,* **127,** 133–137.

Gómez-García, A.M., Le Breton, E., Scheck-Wenderoth, M., Monsalve, G. & Anikiev, D., 2021. The preserved plume of the Caribbean Large Igneous Plateau revealed by 3D data-integrative models, *Solid Earth,* **12,** 275–298.

Gómez-Ortiz, D. & Agarwal, B.N.P., 2005. 3DINVER.M: a MATLAB program to invert the gravity anomaly over a 3D horizontal density interface by Parker–Oldenburg's algorithm, *Comput. Geosci.,* **31,** 513–520.

Gómez-Ortiz, D., Tejero-López, R., Babín-Vich, R. & Rivas-Ponce, A., 2005. Crustal density structure in the Spanish Central System derived from gravity data analysis (Central Spain), *Tectonophysics,* **403,** 131–149.

Graterol, V. & Vargas, A., 2010. Mapa de anomalia de Bouguer total de la Republica de Colombia. ANH (Agencia Nac. Hidrocarburos Colomb. Bogota Magna/Colombia-Magna Bogota Zo. 1850000).

Gutscher, M.A., Malavieille, J., Lallemand, S. & Collot, J.Y., 1999. Tectonic segmentation of the North Andean margin: impact of the Carnegie Ridge collision, *Earth planet. Sci. Lett.,* **168,** 255–270.

Horton, B.K., Parra, M. & Mora, A., 2020. Construction of the Eastern Cordillera of Colombia: insights from the sedimentary record, in *The Geology of Colombia,* Vol. 3, pp. 67–88, eds Gómez, J. & Mateus–Zabala, D., Servicio Geológico Colombiano

Ince, E.S., Barthelmes, F., Reißland, S., Elger, K., Förste, C., Flechtner, F. & Schuh, H., 2019. ICGEM—15 years of successful collection and distribution of global gravitational models, associated services and future plans, *Earth Syst. Sci. Data Discuss.,* 1–61. https://doi.org/10.5194/essd-2019-17.

Karabulut, H., Paul, A., Erg, T.A., Hatzfeld, D., Childs, D.M. & Aktar, M., 2013. Long-wavelength undulations of the seismic Moho beneath the strongly stretched Western Anatolia, *Geophys. J. Int.,* **194**(1), 450–464.

Kay, S.M., Mpodozis, C. & Gardeweg, M., 2014. Magma sources and tectonic setting of Central Andean andesites (25.5-28°S) related to crustal thickening, forearc subduction erosion and delamination, *Geol. Soc. Spec. Publ.,* **385,** 303–334.

Kellogg, J.N., Camelio, G.B.F. & Mora-Páez, H., 2019. Cenozoic tectonic evolution of the North Andes with constraints from volcanic ages, seismic reflection, and satellite geodesy, in *Andean Tectonics,* pp. 69–102, eds Horton, B.K. & Folguera, A., Elsevier.

Kerr, A.C., Marriner, G.F., Tarney, J., Nivia, A., Saunders, A.D., Thirlwall, M.F. & Sinton, C.W., 1997. Cretaceous Basaltic Terranes in Western Colombia: Elemental, *Chronological and Sr-Nd Isotopic Constraints on Petrogenesis. J. Petrol.,* **38,** 677–702, doi.org/10.1093/petrology/38.6.677.

Koch, C.D. *et al.*, 2021. Crustal thickness and magma storage beneath the Ecuadorian arc, *J. South Am. Earth Sci.,* **110,** 103331.

Larkin, S.P., Levander, A., Henstock, T.J. & Pullammanappallil, S., 1997. Is the Moho flat ? Seismic evidence for a rough crust–mantle interface beneath the northern Basin and Range, *Geology,* **25,** 451–454.

Laske, G., Masters, G., Ma, Z. & Pasyanos, M., 2013. Update on CRUST1.0—a 1-degree global model of Earth's crust, *EGU Gen. Assem.,* **15,** 2658.

León, S. *et al.*, 2018. Transition from collisional to subduction-related regimes: an example from Neogene Panama-Nazca-South America interactions, *Tectonics,* **37,** 119–139.

León, S., Monsalve, G. & Bustamante, C., 2021. How much did the Colombian Andes rise by the collision of the Caribbean oceanic plateau?, *Geophys. Res. Lett.,* **48,** 1–11.

Lonsdale, P., 2005. Creation of the Cocos and Nazca plates by fission of the Farallon plate, *Tectonophysics,* **404,** 237–264.

Marín-Cerón, M.I., Leal-Mejía, H., Bernet, M. & Mesa-García, J., 2019. Late Cenozoic to modern-day volcanism in the Northern Andes: a geochronological, petrographical, and geochemical review, in *Geology and Tectonics of Northwestern South America. Frontiers in Earth Sciences,* pp. 603–648, eds Cediel, F. & Shaw, R.P., Springer.

Monsalve, G., Jaramillo, J.S., Cardona, A., Schulte-Pelkum, V., Posada, G., Valencia, V. & Poveda, E., 2019. Deep crustal faults, shear zones, and magmatism in the Eastern Cordillera of Colombia: growth of a plateau

Downloaded from https://academic.oup.com/gji/article/229/3/1964/6521443 by Geoforschungszentrum Potsdam user on 18 May 2022

from teleseismic receiver function and geochemical Mio-Pliocene volcanism constraints, *J. geophys. Res.,* **124,** 9833–9851.

Monsalve, H., Pacheco, J.F., Vargas, C.A. & Morales, Y.A., 2013. Crustal velocity structure beneath the western Andes of Colombian using receiver-function inversion, *J. South Am. Earth Sci.,* **48,** 106–122.

Monsalve-Bustamante, M.L., 2020. The volcanic front in Colombia: segmentation and recent and historical activity, in *The Geology of Colombia,* Vol. 4, pp. 97–159, eds Gómez, J. & Pinilla-Pachon, A.O., Servicio Geológico Colombiano.

Montes, C., Rodriguez-Corcho, A.F., Bayona, G., Hoyos, N., Zapata, S. & Cardona, A., 2019. Continental margin response to multiple arc-continent collisions: the northern Andes-Caribbean margin, *Earth-Sci. Rev.,* **198,** 102903.

Mooney, W.D., 2021. The Moho discontinuity, in *Encyclopedia of Geology,* 2nd edn, pp. 732–743, eds Alderton, D. & Elias, S.A., Elsevier Inc.

Mora, A. *et al.*, 2013. Inversion tectonics under increasing rates of shortening and sedimentation: Cenozoic example from the Eastern Cordillera of Colombia, *Geol. Soc. Spec. Publ.,* **377,** 411–442.

Mora-Páez, H. *et al.*, 2019. Crustal deformation in the northern Andes—a new GPS velocity field, *J. South Am. Earth Sci.,* **89,** 76–91.

Mora-Páez, H., Mencin, D.J., Molnar, P., Diederix, H., Cardona-Piedrahita, L., Peláez-Gaviria, J.R. & Corchuelo-Cuervo, Y., 2016. GPS velocities and the construction of the Eastern Cordillera of the Colombian Andes, *Geophys. Res. Lett.,* **43,** 8407–8416.

Oldenburg, D.W., 1974. The inversion and interpretation of gravity anomalies, *Geophysics,* **39,** 526–536.

Pardo-Trujillo, A. *et al.*, 2020. Sedimentary record of the Cretaceous–Paleocene arc–continent collision in the northwestern Colombian Andes: insights from stratigraphic and provenance constraints, *Sediment. Geol.,* **401,** 105627.

Parker, R.L., 1973. The rapid calculation of potential anomalies, *Geophys. J. R. astr. Soc.,* **31,** 447–455.

Parra, M., Mora, A., Lopez, C., Rojas, L.E. & Horton, B.K., 2012. Detecting earliest shortening and deformation advance in thrust belt hinterlands: example from the Colombian Andes, *Geology,* **40,** 175–178.

Pavlis, N.K., Holmes, S.A., Kenyon, S.C. & Factor, J.K., 2012. The development and evaluation of the Earth Gravitational Model 2008 (EGM2008), *J. geophys. Res.,* **117,** 1–38.

Poveda, E., 2013. *Discontinuidades sísmicas en la litósfera bajo la zona andina y el occidente colombianos a partir de formas de onda de sismos distantes,* Universidad Nacional de Colombia.

Poveda, E., Julià, J., Schimmel, M. & Perez-Garcia, N., 2018. Upper and middle crustal velocity structure of the Colombian Andes from ambient noise tomography: investigating subduction-related magmatism in the overriding plate, *J. geophys. Res.,* **123,** 1459–1485.

Poveda, E., Monsalve, G. & Vargas, C.A., 2015. Receiver functions and crustal structure of the northwestern Andean region, Colombia, *J. geophys. Res.,* **120,** 2408–2425.

Prasanna, H.M.I., Chen, W. & Iz, H.B., 2013. High resolution local Moho determination using gravity inversion: a case study in Sri Lanka, *J. Asian Earth Sci.,* **74,** 62–70.

Reguzzoni, M. & Sampietro, D., 2015. GEMMA: an Earth crustal model based on GOCE satellite data, *Int. J. Appl. Earth Obs. Geoinf.,* **35,** 31–43.

Saeid, E., Bakioglu, K.B., Kellogg, J., Leier, A., Martinez, J.A. & Guerrero, E., 2017. Garzón Massif basement tectonics: structural control on evolution of petroleum systems in upper Magdalena and Putumayo basins, Colombia, *Mar. Pet. Geol.,* **88,** 381–401.

Sahoo, S.D. & Pal, S.K., 2021. Crustal structure and Moho topography of the southern part (18°S–25°S) of Central Indian Ridge using high-resolution EIGEN6C4 global gravity model data, *Geo-Marine Lett.,* **41,** https://doi.org/10.1007/s00367-020-00679-z.

Sarmiento-Rojas, L.F., 2019. Cretaceous stratigraphy and paleo-facies maps of Northwestern South America, in *Geology and Tectonics of Northwestern South America. Frontiers in Earth Sciences,* eds Cediel, F. & Shaw, R.P., Springer, https://doi.org/10.1007/978-3-319-76132-9_10.

Schreiber, D., Lardeaux, J.M., Martelet, G., Courrioux, G. & Guillen, A., 2010. 3-D modelling of Alpine Mohos in Southwestern Alps, *Geophys. J. Int.,* **180,** 961–975.

Shi, Z., Gao, R., Li, W., Lu, Z. & Li, H., 2020. Cenozoic crustal-scale duplexing and flat Moho in southern Tibet: evidence from reflection seismology, *Tectonophysics,* **790,** 228562.

Siravo, G., Faccenna, C., Gérault, M., Becker, T.W., Fellin, M.G., Herman, F. & Molin, P., 2019. Slab flattening and the rise of the Eastern Cordillera, Colombia, *Earth planet. Sci. Lett.,* **512,** 100–110.

Siravo, G., Fellin, M.G., Faccenna, C., Bayona, G., Lucci, F., Molin, P. & Maden, C., 2018. Constraints on the Cenozoic deformation of the Northern Eastern Cordillera, Colombia, *Tectonics,* **37,** 4311–4337.

Sjöberg, L.E. & Bagherbandi, M., 2011. A method of estimating the Moho density contrast with a tentative application of EGM08 and CRUST2.0, *Acta Geophys.,* **59,** 502–525.

Spada, M., Bianchi, I., Kissling, E., Agostinetti, N.P. & Wiemer, S., 2013. Combining controlled-source seismology and receiver function information to derive 3-D Moho topography for Italy, *Geophys. J. Int.,* **194,** 1050–1068.

Syracuse, E.M., Maceira, M., Prieto, G.A., Zhang, H. & Ammon, C.J., 2016. Multiple plates subducting beneath Colombia, as illuminated by seismicity and velocity from the joint inversion of seismic and gravity data, *Earth planet. Sci. Lett.,* **444,** 139–149.

Thybo, H. & Artemieva, I.M., 2013. Moho and magmatic underplating in continental lithosphere, *Tectonophysics,* **609,** 605–619.

Tirel, C., Gueydan, F., Tiberi, C. & Brun, J.P., 2004. Aegean crustal thickness inferred from gravity inversion, Geodynamical implications, *Earth planet. Sci. Lett.,* **228,** 267–280.

Uieda, L. & Barbosa, V.C.F., 2017. Fast nonlinear gravity inversion in spherical coordinates with application to the South American Moho, *Geophys. J. Int.,* **208,** 162–176.

van der Meijde, M., Julià, J. & Assumpção, M., 2013. Gravity derived Moho for South America, *Tectonophysics,* **609,** 456–467.

Vargas, C.A., 2020. Subduction geometries in northwestern South America, in *The Geology of Colombia,* Vol. 4, pp. 397–422, eds Gómez, J. & Pinilla–Pachon, A.O., Servicio Geológico Colombiano.

Vargas, C.A. & Mann, P., 2013. Tearing and breaking off of subducted slabs as the result of collision of the panama arc-indenter with Northwestern South America, *Bull. seism. Soc. Am.,* **103,** 2025–2046.

Veloza, G., Styron, R. & Taylor, M., 2012. Open-source archive of active faults for northwest South America, *GSA Today,* **22,** 4–10.

Villagómez, D. & Spikings, R., 2013. Thermochronology and tectonics of the Central and Western Cordilleras of Colombia: early Cretaceous-Tertiary evolution of the Northern Andes, *Lithos,* **160-161,** 228–249.

Wagner, L.S., Jaramillo, J.S., Ramírez-Hoyos, L.F., Monsalve, G., Cardona, A. & Becker, T.W., 2017. Transient slab flattening beneath Colombia, *Geophys. Res. Lett.,* **44,** 6616–6623.

Whitman, D., 1994. Moho geometry beneath the eastern margin of the Andes, northwest Argentina, and its implications to the effective elastic thickness of the Andean foreland, *J. geophys. Res.,* **99,** 15277–15289.

Xuan, S., Jin, S. & Chen, Y., 2020. Determination of the isostatic and gravity Moho in the East China Sea and its implications, *J. Asian Earth Sci.,* **187,** 104098.

Yarce, J., Monsalve, G., Becker, T.W., Cardona, A., Poveda, E., Alvira, D. & Ordoñez-Carmona, O., 2014. Seismological observations in Northwestern South America: evidence for two subduction segments, contrasting crustal thicknesses and upper mantle flow, *Tectonophysics,* **637,** 57–67.

Ydri, A., Idres, M., Ouyed, M. & Samai, S., 2020. Moho geometry beneath northern Algeria from gravity data inversion, *J. Afr. Earth Sci.,* **168,** 103851.

SUPPORTING INFORMATION

Supplementary data are available at *GJI* online.

Supplementary Table S1.xls

Please note: Oxford University Press is not responsible for the content or functionality of any supporting materials supplied by the authors. Any queries (other than missing material) should be directed to the corresponding author for the paper.

Downloaded from https://academic.oup.com/gji/article/229/3/1964/6521443 by Geoforschungszentrum Potsdam user on 18 May 2022